

# Electrical Control of Magnetic Behavior and Valley Polarization of Monolayer Antiferromagnetic MnPSe<sub>3</sub> on an Insulating Ferroelectric Substrate from First Principles

Qi Pei and Wenbo Mi\*

Tianjin Key Laboratory of Low Dimensional Materials Physics and Preparation Technology, School of Science, Tianjin University, Tianjin 300354, China



(Received 8 August 2018; revised manuscript received 1 December 2018; published 7 January 2019)

The manipulation of magnetism and valley has vital applications in multifunctional spintronic and valleytronic devices. Coupling the valley degree of freedom of a two-dimensional (2D) magnet to the ferroelectricity of multiferroic materials offers exciting opportunities to achieve challenging electrically controlled valleytronics. Meanwhile, the magnetic behavior of 2D materials can also be tailored for magnetoelectric coupling. The proposed valley-ferroelectricity coupling is predicted in monolayer MnPSe<sub>3</sub> on top of a YMnO<sub>3</sub> (001) substrate. The results show that the magnitude of valley polarization and the conductivity of monolayer MnPSe<sub>3</sub> are closely correlated with YMnO<sub>3</sub> terminations. The valley polarization modulations in MnO-terminated heterostructures can reach 46 meV when the ferroelectric polarization is reversed. Furthermore, owing to the exchange interaction between MnPSe<sub>3</sub> and the topmost surface atoms, the magnetism of monolayer MnPSe<sub>3</sub> in O<sub>2-</sub> and MnO-terminated models can be effectively modulated with polarization switching. The electrical control of magnetic behavior and valley polarization in MnPSe<sub>3</sub>-YMnO<sub>3</sub> paves the way for developing nonvolatile data memories, where the magnetization and valley pseudospin are both involved in the memory elements.

DOI: 10.1103/PhysRevApplied.11.014011

## I. INTRODUCTION

With the discovery of graphene, the concept of valleytronics has been proposed and paid considerable attention in recent years [1–3]. Valleytronics relies on carriers capable of carrying a valley degree of freedom (valley pseudospin) [4]. This electronic degree of freedom results in unconventional valley physics and potential applications in spintronic and valleytronic devices [5]. In order to utilize the valley degree of freedom, the key factors are the generation and manipulation of valley polarization. Optical pumping with circular polarized light has been used to generate the valley degeneracy of transition-metal dichalcogenides (TMDCs) on the basis of valley-selective circular dichroism [6–8]. However, optical pumping is susceptible as a dynamic process, where the achieved valley polarization is subjected to the lifetime of carriers. Thus, the optical approach is difficult to robustly manipulate and is not suitable for practical information storage. By the magnetic doping [9–11] or proximity to magnetic substrates [12,13], the valley polarization can also be tailored, which offers new paradigms for valleytronics. However, the induced dopants were liable to form clusters and increased the scattering rate, and thus they were detrimental to the

device performance [14]. Equipping these devices with a magnetic field generator greatly increases the size and energy consumption of the devices. Thus, it is important to explore new options for manipulating the valley polarization.

Electric-field control of high-performing materials is an exciting topic toward the innovation of multifunctional spintronic and valleytronic devices [15]. Multiferroics, which integrates ferroelectricity and magnetic properties, provides the possibility for the charge and spin modulations by applying a voltage. The electronic devices based on the ferroelectric materials have many physical advantages such as high integration, low energy consumption, and fast response. So far, much work involving multiferroics has focused on electrical control of the magnetism [16–19], while few studies are devoted to the modulation of valley degree of freedom by an electric field. Concerning the convenience and effectiveness of electric-field control, the multiferroic intermediate is an innovating strategy toward electrical control on valley pseudospin, which is a superior approach compared to the traditional magnetic one. In addition, the profusion of two-dimensional (2D) materials with a honeycomb lattice introduces the transition-metal trichalcogenide monolayers into our vision [20]. Exemplified by monolayer MnPSe<sub>3</sub>, this intrinsic antiferromagnetic (AFM) semiconductor shows

\*miwenbo@tju.edu.cn

a direct band gap, which falls well within the optical absorption range [21,22]. Li *et al.* [23] have proposed spontaneous valley polarization in monolayer MnPSe<sub>3</sub> with the noncollinear treatment of magnetism, which satisfies the demand of lifting valley degeneracy and opens an energy window for anomalous spin Hall effect with equilibrium *n* or *p* doping [24]. Hence, monolayer MnPSe<sub>3</sub> is a suitable research object to realize the electrical control of valley polarization. In addition, the magnetic behavior of MnPSe<sub>3</sub> on a ferroelectric substrate may also be affected by magnetoelectric coupling.

In this work, we deposit the AFM monolayer MnPSe<sub>3</sub> on an insulating ferroelectric YMnO<sub>3</sub> substrate to construct the MnPSe<sub>3</sub>-YMnO<sub>3</sub> heterostructures. By systematically investigating the influences of substrate termination and ferroelectric polarization on the electronic properties and magnetic behavior of MnPSe<sub>3</sub>, we find that different substrate terminations can modulate the strength of interfacial hybridization, switching the *p*- or *n*-type doping of MnPSe<sub>3</sub>. The proposed electrically tailored valley polarization is predicted in MnO-terminated heterostructures, which can be changed by 46 meV with ferroelectric polarization reversal. Meanwhile, the exchange coupling between AFM MnPSe<sub>3</sub> and the adjacent ferroelectric YMnO<sub>3</sub> creates the termination-polarization dependence of magnetism in monolayer MnPSe<sub>3</sub>, suggesting promising applications in electrically writing and magnetically reading memory devices.

## II. CALCULATION DETAILS

Density functional theory (DFT) calculations are performed by using Vienna *ab initio* simulation package (VASP) code [25,26] with a generalized gradient approximation parameterized by Perdew-Burke-Ernzerhof [27]. Van der Waals corrections are considered within the Grimme's method (DFT-D2) [28] for the longer-ranged correlation. The criteria of energy and atom force convergence are less than 10<sup>-5</sup> eV and 0.01 eV/Å, respectively. The

plane-wave kinetic-energy cutoff is 500 eV. A 20-Å-thick vacuum layer along the *z* axis is employed to minimize the interaction between the periodic images and a dipole correction was applied [29]. A 5 × 5 × 1 Monkhorst-Pack grid is used for the *k* point sampling in the Brillouin zone. To properly account for the strongly correlated systems with partially filled *d* subshells, the effective onsite coulomb (*U*) and exchange (*J*) interactions are set as suggested in the literature (*U* = 5 eV, *J* = 0 eV for Mn components in monolayer MnPSe<sub>3</sub>; *U* = 8.0 eV, *J* = 0.88 eV for Mn in YMnO<sub>3</sub>) [30–33]. Spin-orbit coupling (SOC) is considered in the electronic structure calculations.

## III. RESULTS AND DISCUSSION

### A. Properties of bulk YMnO<sub>3</sub> and monolayer MnPSe<sub>3</sub>

Bulk YMnO<sub>3</sub> has a hexagonal structure alternating between the layers of Y<sup>3+</sup> ions and the nonconnected layers of MnO<sub>5</sub> trigonal bipyramids. Previous work revealed that the buckling of the MnO<sub>5</sub> polyhedral accompanied by the displacements of Y<sup>3+</sup> ions played a major role in the origin of ferroelectricity [34]. The underlying mechanism was further elucidated as the electrostatic and size effects rather than the covalency effects (chemical bonding) in the conventional perovskite oxides [35]. The ferroelectric Curie temperature of approximately 900 K [36] is much higher than its Néel temperature of 75 K [37]. Below the Néel temperature, an AFM ordering oriented with the noncollinear Mn spins appears. Solovyev *et al.* [38] calculated the total energies of YMnO<sub>3</sub> with six possible spin configurations 1–6, and proved that 3 with the magnetic space group of *P*<sub>6</sub><sub>3</sub>*cm* was the ground state. This theoretical result was also in good agreement with the experimental finding [39]. Therefore, the 3 configuration shown in Fig. 1(b) is selected in our simulation process. Then the band structure (BS) and density of states (DOS) are calculated to reproduce the electronic properties of YMnO<sub>3</sub>. Figure 1(c) shows a typical semiconductor-like band for YMnO<sub>3</sub>. The band gap of approximately 1.60 eV

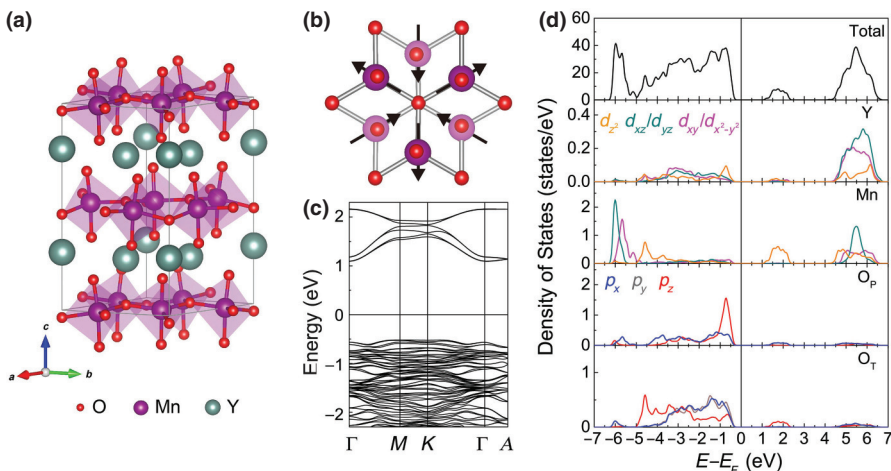


FIG. 1. (a) The crystal structure of bulk YMnO<sub>3</sub> in the ferroelectric phase. (b) The magnetic structure of  $\Gamma$ 3 with magnetic space group of *P*<sub>6</sub><sub>3</sub>*cm*. The spin orientation is depicted by the black arrows. (c) BS and (d) total and orbital-resolved DOS of bulk YMnO<sub>3</sub>. Fermi level is indicated by the black line and set to zero. O<sub>p</sub> and O<sub>t</sub> denote the in-plane and apical O atoms of the MnO<sub>5</sub> polyhedral, respectively.

is comparable with the optical gap of 1.55 eV in experiments [40]. The insulating state is strongly relevant to the spin frustration. In the Mn-O triangular bipyramidal hexagonal YMnO<sub>3</sub>, Mn 3d states split into two *e*<sub>1g</sub> orbitals (*d*<sub>xz</sub>, *d*<sub>yz</sub>) with the lowest level and two *e*<sub>2g</sub> orbitals (*d*<sub>xy</sub>, *d*<sub>x<sup>2</sup>-y<sup>2</sup></sub>) and one singlet *a*<sub>1g</sub> (*d*<sub>z<sup>2</sup></sub>) with the highest energy. In Fig. 1(d), O 2p orbitals make the most contribution to the highest occupied level, while the lowest unoccupied level above 1 eV has the Mn 3d (*d*<sub>z<sup>2</sup></sub>) characteristics. In addition, the overlapping DOSs of Mn *d*<sub>z<sup>2</sup></sub> and O 2p states in the energy range from 1.0 to 2.5 eV suggest the bonding picture between the Mn and O ions.

Bulk MnPSe<sub>3</sub> is an AFM magnetic semiconductor with an optical energy of 2.27 eV [41] and a Néel temperature of 74 K [42]. When it is exfoliated to the monolayer, the magnetic ground state of 2D MnPSe<sub>3</sub> remains AFM and the theoretical Néel temperature was predicated to be 88 K [21], close to the value of the bulk system. As shown in Fig. 2(a), the monolayer MnPSe<sub>3</sub> is constituted by two Mn<sup>2+</sup> and one [P<sub>2</sub>Se<sub>6</sub>]<sup>4-</sup> cluster, where the middle Mn ions sandwiched between the side P and Se layers form a honeycomb similar to graphene. Two Mn<sup>2+</sup> ions in one unit cell possess the opposite magnetic moment of approximately 4.6  $\mu_B$ , while P and Se atoms have negligible magnetic moments. Recent theoretical results on the monolayer MnPSe<sub>3</sub> [43] have shown a direct band gap within the optical absorption range, facilitating the optical polarization of charge carriers. When the SOC

effect is considered, the band renormalization lifts the valley degeneracy, and thus spontaneous valley polarization occurs. In Fig. 2(c), two inequivalent valleys (*K* and *K'*) are localized at the corners of the first Brillouin zone. In the system with valley degree of freedom, the valley polarization can be quantified by the energy differences between the valleys at *K* and *K'* in valence bands ( $\Delta_{\text{val}}$ ) and conduction bands ( $\Delta_{\text{val}}^C$ ), denoted as  $\Delta_{\text{val}}^{C/V} = E_K^{C/V} - E_{K'}^{C/V}$ . In the monolayer MnPSe<sub>3</sub>, two energy windows  $\Delta_{\text{val}}^V$  and  $\Delta_{\text{val}}^C$  are about -20 and 36 meV, respectively. From the orbital-resolved DOS, it can be concluded that the valence band maximum (VBM) states of monolayer MnPSe<sub>3</sub> are mainly contributed by Se *p* and Mn *d* orbitals, whereas the conduction band minimum (CBM) consists of the Se *p* orbital mixed with P *p* and Mn *d* states.

## B. Interface structures

Based on the optimized structures, the in-plane lattice constants for monolayer MnPSe<sub>3</sub> and bulk YMnO<sub>3</sub> are 6.403 and 6.137 Å, respectively. Hence, the lattice of a  $1 \times 1 \times 1$  MnPSe<sub>3</sub> monolayer can be closely matched to the  $1 \times 1$  lattice of YMnO<sub>3</sub> (001) film with a lattice mismatch of 4.2%. Our previous work [44] showed that a 5% compressive strain barely changed the basic band features of monolayer MnPSe<sub>3</sub> except for a decreased band gap, so the in-plane lattice constants of interface structures are fixed to the values of the YMnO<sub>3</sub> (001) slab.

To begin with, four possible top surfaces with two ferroelectric polarizations of YMnO<sub>3</sub> (001) substrates, terminating symmetrically on O1, Y, O2, and MnO atoms, are considered to construct the MnPSe<sub>3</sub>-YMnO<sub>3</sub> heterostructures. Here, O1 and O2 refer to the top and bottom layers of oxygen atoms in MnO<sub>5</sub> trigonal bipyramids, respectively. Figure 3 shows the crystal structures of MnPSe<sub>3</sub>-YMnO<sub>3</sub> heterostructures before geometric optimization. The subscript “up” (“dn”) represents the ferroelectric polarization of YMnO<sub>3</sub> pointing to (away from) the interface. The MnPSe<sub>3</sub>-YMnO<sub>3</sub> heterostructures are named O1<sub>up</sub>, O1<sub>dn</sub>, Y<sub>up</sub>, Y<sub>dn</sub>, O2<sub>up</sub>, O2<sub>dn</sub>, MnO<sub>up</sub>, and MnO<sub>dn</sub> in sequence. From the symmetry point of view, O1- and O2-terminated models have 11 atomic layers, while Y and MnO terminations are nine layer slabs. The atoms at the bottom three layers of the YMnO<sub>3</sub> substrate are fixed at its bulk positions.

After geometric optimization, the cohesive energy calculations are performed to explore the stability by using  $W_{\text{coh}} = E_{\text{MnPSe}_3} + E_{\text{YMnO}_3} - E_{\text{MnPSe}_3-\text{YMnO}_3}$ , where  $E_{\text{MnPSe}_3-\text{YMnO}_3}$ ,  $E_{\text{MnPSe}_3}$ , and  $E_{\text{YMnO}_3}$  denote the total energies of the heterostructure, monolayer MnPSe<sub>3</sub>, and YMnO<sub>3</sub> slab, respectively. For Y-, O2-, and MnO-terminated models, the values of  $W_{\text{coh}}$  are within the range of 0.75–2.27 eV, comparable to those of other 2D materials on magnetic substrates [13,45]. Based on the definition of the equation, the structure with a larger  $W_{\text{coh}}$  is more stable.

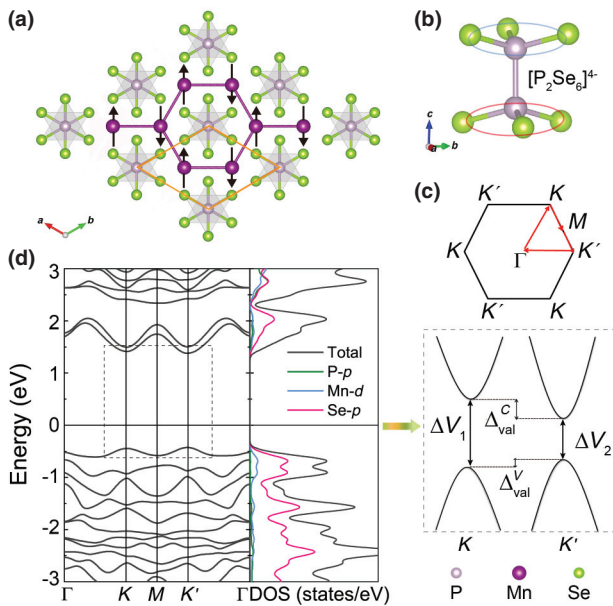


FIG. 2. (a) Top view of monolayer MnPSe<sub>3</sub>. Up (down) spins are denoted by the black up (down) arrows. The unit cell is indicated by the orange solid line. (b) Side view of [P<sub>2</sub>Se<sub>6</sub>]<sup>4-</sup> unit in MnPSe<sub>3</sub>. (c) First Brillouin zone and high symmetry points. (d) BS and DOS of monolayer MnPSe<sub>3</sub>. The schematic diagram of BS at *K* and *K'* valleys is also plotted in (d).

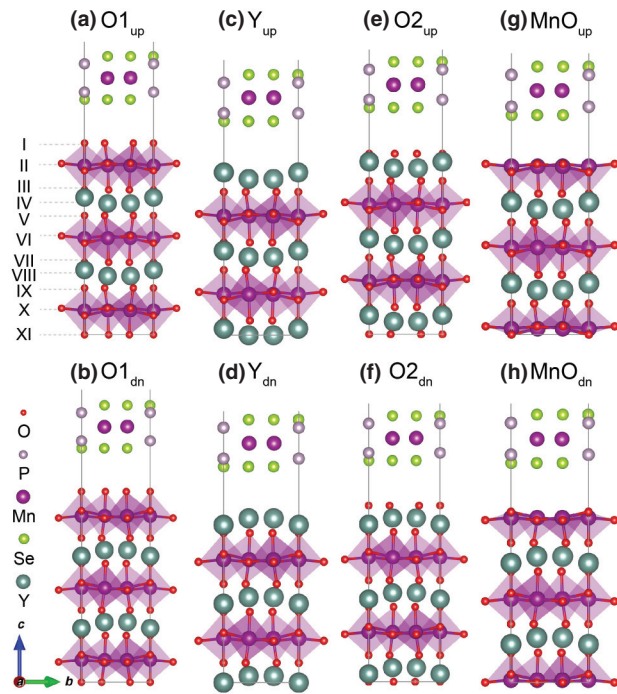


FIG. 3. Side views of (a)  $O1_{up}$ , (b)  $O1_{dn}$ , (c)  $Y_{up}$ , (d)  $Y_{dn}$ , (e)  $O2_{up}$ , (f)  $O2_{dn}$ , (g)  $MnO_{up}$ , and (h)  $MnO_{dn}$  before geometric optimization.

One can notice that the most stable and unstable configurations are both assigned to MnO-terminated models with different polarization directions, which reveals that the ferroelectric polarization of  $YMnO_3$  may have a vital influence on the interfacial interaction between the monolayer  $MnPSe_3$  and  $YMnO_3$  substrates. Notably, although the small positive  $W_{coh}$  values are obtained for O1-terminated models, the obvious structural distortion appears in both  $O1_{up}$  and  $O1_{dn}$  when comparing the configurations before and after geometric optimization (shown in Fig. S1 of the Supplemental Material [46]), and thus O1-terminated models might not appear during the preparation and are not involved in the following discussions.

TABLE I. The calculated cohesive energies ( $W_{coh}$ ), interfacial distances between the topmost layer and the lower Se layer ( $d_0$ ), valley polarization in conduction ( $\Delta_{val}^C$ ) and valance ( $\Delta_{val}^V$ ) bands for the pristine  $MnPSe_3$  and  $MnPSe_3/YMnO_3$  heterostructures, magnetic moment components of two Mn atoms in  $MnPSe_3$  along  $x$ ,  $y$ , and  $z$  directions, and magnetic moments (total and components along  $x$ ,  $y$ , and  $z$  directions) of monolayer  $MnPSe_3$ .

	$W_{coh}$ (eV)	$d_0$ (Å)	$\Delta_{val}^C$ (meV)	$\Delta_{val}^V$ (meV)	$M_{Mn1}$ ( $x-y-z$ ) ( $\mu_B$ )	$M_{Mn2}$ ( $x-y-z$ ) ( $\mu_B$ )	$M$ ( $x-y-z$ ) ( $\mu_B$ )	$M$ Total ( $\mu_B$ )
$MnPSe_3$	-	-	36	-20	0/0/4.57	0/0/-4.57	0/0/0	0
$Y_{up}$	0.84	2.21	67	-	0/0/4.53	0/0/-4.53	0/0/0	0
$Y_{dn}$	1.30	2.56	49	-	0/0/4.52	0/0/-4.52	0/0/0	0
$O2_{up}$	1.11	2.23	29	-	0.14/-0.06/4.52	-0.13/-0.15/-4.54	0/-0.17/-0.03	0.17
$O2_{dn}$	1.04	2.42	31	-	-0.02/0.02/4.51	-0.01/0.04/-4.55	-0.03/0.04/-0.18	0.19
$MnO_{up}$	2.27	2.69	31	1	-0.12/0.37/4.55	-0.03/0.32/-4.55	-0.16/0.70/0	0.72
$MnO_{dn}$	0.75	2.60	29	-45	0.09/0.12/4.56	0.07/0.06/-4.56	0.16/0.18/0	0.24

We define the separation between the surface atoms and bottom Se layer as the equilibrium interfacial distance  $d_0$ . To a certain extent,  $d_0$  can reflect the strength of interfacial bonding. As listed in Table I, the values of  $d_0$  of MnO-terminated heterostructures are slightly larger than those of Y- and O2-terminated models, implying a weak interfacial hybridization. Moreover,  $d_0$  is sensitive to the ferroelectric polarization switching. The difference in  $d_0$  between  $Y_{up}$  and  $Y_{dn}$  can be up to 0.35 Å.

In order to visualize the bonding feature at the interfaces, the charge density difference is calculated by subtracting the charge densities of the isolated  $MnPSe_3$  and substrate from the heterostructures. The electronic structures of the isolated monolayer  $MnPSe_3$  and  $YMnO_3$  (001) substrate are calculated by freezing the corresponding atomic positions in the heterostructures. In Figs. 4(a) and 4(b), the charge redistributes not only at the interface, but also inside the monolayer  $MnPSe_3$ . By switching the ferroelectric polarization, the Y atoms in the first layer (denoted as I-Y) for  $Y_{up}$  and  $Y_{dn}$  have an obvious change in position. The charge depletes around the interfacial Se-Y bond with the shortest length, showing a covalent characteristic. For the O2-terminated heterostructures shown in Figs. 4(c) and 4(d), obvious charge transfer from Se to O2 atoms can be observed. For the MnO-terminated models, the ionic interaction leads to the interfacial charge redistributions, with the charge transfer from interfacial Se to the topmost MnO layer. The changes in termination and ferroelectric polarization are both responsible for the structure and charge modulations.

### C. Tunable magnetic behavior in $MnPSe_3-YMnO_3$ heterostructures

The total magnetic moment of pristine monolayer  $MnPSe_3$  is 0  $\mu_B$  owing to the collinear AFM configuration, while after being deposited on the  $YMnO_3$  substrate, the magnetic behavior of monolayer  $MnPSe_3$  changes significantly. As listed in Table I, for Y-terminated models, the magnetic moment of a Mn atom in  $MnPSe_3$  is still arranged

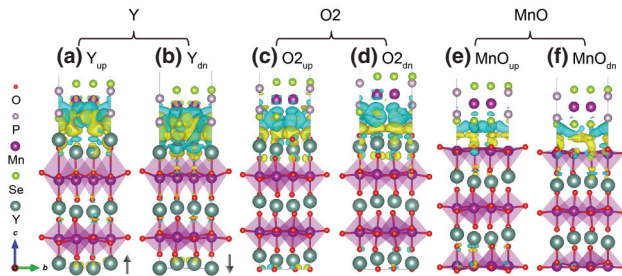


FIG. 4. Charge-density difference of (a)  $Y_{up}$ , (b)  $Y_{dn}$ , (c)  $O2_{up}$ , (d)  $O2_{dn}$ , (e)  $MnO_{up}$ , and (f)  $MnO_{dn}$ . The isosurface value is  $1 \text{ e}/\text{nm}^3$  for (a)-(d), but for (e) and (f), this value is set to be  $0.5 \text{ e}/\text{nm}^3$ . The yellow (blue) region represents net charge gain (loss).

along the  $z$  axis. The total magnetic moment of monolayer  $\text{MnPSe}_3$  remains  $0 \mu_B$ . Given that the surface Y atoms are nonmagnetic [34], the relatively weak magnetic coupling between  $\text{MnPSe}_3$  and the Y-terminated substrate is not sufficient to influence the magnetic behavior of  $\text{MnPSe}_3$ .

For the  $O2$ -terminated models, the magnetic moment of each Mn atom has components in three directions. The weak magnetism is introduced in the monolayer  $\text{MnPSe}_3$ . Moreover, the magnitude of total moment of  $\text{MnPSe}_3$  can be changed from  $0.17$  to  $0.19 \mu_B$  by reversing the ferroelectric polarization. Considering that the additional Mn atoms from the  $\text{YMnO}_3$  substrate are far from monolayer  $\text{MnPSe}_3$ , the changes in magnetic properties of  $\text{MnPSe}_3$  are most likely due to the influence from surface  $O2$  atoms. For a clean  $O2$ -terminated substrate with a positive polarization, the moments of the surface  $O2$  atoms are  $0.19$ ,  $0.20$ , and  $0.20 \mu_B$ . When the polarization of the substrate is reversed, three  $O2$  atoms have magnetic moments of  $0.06$ ,  $0.19$ , and  $0.06 \mu_B$ . We determine that the surface  $O2$  atoms in clean substrates are intrinsically magnetic and they are sizable enough to influence the moments of  $\text{MnPSe}_3$ . After contact with monolayer  $\text{MnPSe}_3$ , the moments of three surface  $O2$  atoms change to  $0.07$ ,  $0.07$ , and  $0.11 \mu_B$  ( $0.11$ ,  $0.10$ , and  $0.07 \mu_B$ ) in the  $O2_{up}$  ( $O2_{dn}$ ) heterostructure. The weak magnetism in monolayer  $\text{MnPSe}_3$  can be ascribed to the exchange interaction between  $\text{MnPSe}_3$  and surface  $O2$  atoms.

For the  $\text{MnO}$ -terminated models, the induced magnetic moments of  $\text{MnPSe}_3$  by magnetoelectric coupling have no components in the  $z$  direction, where the values in  $\text{MnO}_{up}$  and  $\text{MnO}_{dn}$  are  $0.72$  and  $0.24 \mu_B$ , respectively. In addition, the in-plane magnetic moments also depend on the ferroelectric polarization, which can rotate by an angle of  $53.7^\circ$  from the second quadrant to the first quadrant in  $x$ - $y$  coordinates with the ferroelectric polarization reversal. Then, the effect of surface Mn (denoted as  $\text{Mn}_{\text{YMnO}_3}$ ) and O atoms on the magnetic properties of  $\text{MnPSe}_3$  is considered. We find the variation of exchange interactions between Mn in  $\text{MnPSe}_3$  (denoted as  $\text{Mn}_{\text{MnPSe}_3}$ ) and

$\text{Mn}_{\text{YMnO}_3}$  is negligible compared to that between surface O and  $\text{Mn}_{\text{MnPSe}_3}$ . To be specific, the variations of magnetic moments of surface  $\text{Mn}_{\text{YMnO}_3}$  atoms are  $0.003$ ,  $-0.028$ , and  $-0.020 \mu_B$  when the polarization of the substrate is reversed. These values are in the same order of magnitude as that of surface O atoms, which are  $0.007$ ,  $-0.078$ , and  $0.038 \mu_B$ . However, the variations of O– $\text{Mn}_{\text{MnPSe}_3}$  distances with polarization reversal are an order of magnitude larger than that of  $\text{Mn}_{\text{MnPSe}_3}$ – $\text{Mn}_{\text{YMnO}_3}$  distances. Hence, the major cause of tunable magnetism is the variation of the O– $\text{Mn}_{\text{MnPSe}_3}$  distance (O– $\text{Mn}_{\text{MnPSe}_3}$  exchange interaction) rather than the variation of  $\text{Mn}_{\text{MnPSe}_3}$ – $\text{Mn}_{\text{YMnO}_3}$  distances ( $\text{Mn}_{\text{MnPSe}_3}$ – $\text{Mn}_{\text{YMnO}_3}$  exchange interaction). The charge doping effect may also have an impact on the population of Mn atoms, leading to changes in exchange coupling strength. However, based on Bader analysis, the charge transfer is predicted to be  $0.032 e^-$  and  $0.023 e^-$  in  $\text{MnO}_{up}$  and  $\text{MnO}_{dn}$ , respectively, with the direction from  $\text{MnPSe}_3$  to  $\text{YMnO}_3$ . Due to the negligible charge transfer, the charge doping effect in  $\text{MnO}$ -terminated models is not involved in our discussion.

The ferroelectricity tailored magnetic property offers a complementary strategy in producing magnetoelectric random access memories (MERAMs). The magnetoelectric coupling enables the exchange coupling at the interface of  $\text{YMnO}_3$  with  $\text{MnPSe}_3$  to be controlled by an electric field. The binary information is stored by the magnetization of  $\text{MnPSe}_3$ , which could be switched by the ferroelectric polarization of  $\text{YMnO}_3$  through an external electric field, while the information can still be read out by head access. The proposed MERAMs prototype based on electrical writing and magnetic reading has the characteristics of high speed, nonvolatility, and low consumption, extending the potential of multifunctional  $\text{MnPSe}_3$  for future electronic devices access memory. Meanwhile, the same phenomena may also expand to other 2D magnetic materials and ferroelectric heterostructures.

#### D. Electrically controlled valley polarization in $\text{MnPSe}_3$ – $\text{YMnO}_3$ heterostructures

BS for  $\text{MnPSe}_3$ – $\text{YMnO}_3$  heterostructures with three contact terminations is shown in Fig. 5. It is clear that the BS of  $\text{YMnO}_3$  changes significantly with the terminal change and the reversal of ferroelectric polarization. For Y-terminated models in Figs. 5(a) and 5(b), the original bands of monolayer  $\text{MnPSe}_3$  shift to a lower energy region, while the CBM becomes occupied. The resulting  $n$ -type  $\text{MnPSe}_3$  is also in accordance with the Bader analysis, which shows an amount of  $0.86$  ( $0.59$ )  $e^-$  is transferred from  $\text{YMnO}_3$  to  $\text{MnPSe}_3$  in  $Y_{up}$  ( $Y_{dn}$ ). The valley characteristic of monolayer  $\text{MnPSe}_3$  disappears in valence bands due to the strong interfacial hybridization, while  $\Delta_{val}^C$  changes by  $18 \text{ meV}$  with the substrate polarization reversed. In addition, the highest valance band at  $\Gamma$

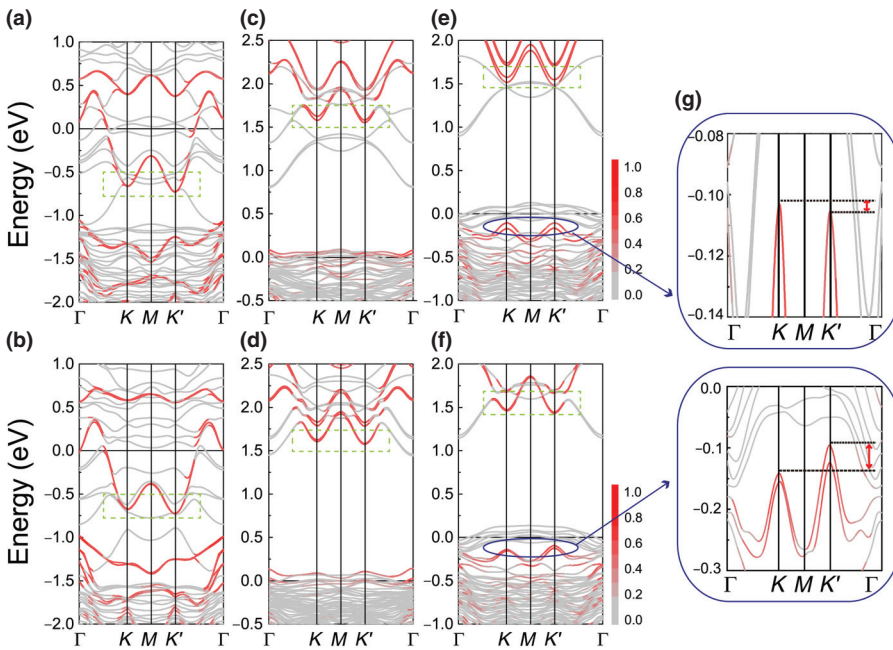


FIG. 5. BS of (a)  $Y_{\text{up}}$ , (b)  $Y_{\text{dn}}$ , (c)  $O_2_{\text{up}}$ , (d)  $O_2_{\text{dn}}$ , (e)  $MnO_{\text{up}}$ , and (f)  $MnO_{\text{dn}}$ . The red (gray) line represents  $MnPSe_3$  ( $YMnO_3$ ) components in heterostructures. (g) Magnified view of the valence bands around the  $K$  and  $K'$  points in MnO-terminated models, corresponding to the solid blue ellipse in (e) and (f).

point becomes the VBM, resulting in the direct to indirect band-gap transition.

Similar to Y-terminated heterostructures,  $\Delta_{\text{val}}^C$  of  $O_2$ -terminated models can also be tuned by switching the ferroelectric polarization. As can be seen in Figs. 5(c) and 5(d), the *p*-type doping of  $MnPSe_3$  appears due to the bottom Se layer losing electrons. The valence bands of monolayer  $MnPSe_3$  have a strong orbital hybridization with  $O_2$  termination, where its valley characteristic is partially destroyed.

For MnO-terminated models, the degenerate valleys can be clearly found both in the conduction and valance bands. As shown in Table I, the  $\Delta_{\text{val}}^V$  in  $MnO_{\text{dn}}$  is predicted to be -45 meV, with a comparable value to the valley polarization of 63 meV in  $WS_2$ -MnO heterostructures [45]. However, when the ferroelectric polarization points to the interface ( $MnO_{\text{up}}$ ), a small reversed  $\Delta_{\text{val}}^V$  of 1 meV appears in  $MnO_{\text{up}}$ . That is to say, the  $\Delta_{\text{val}}^V$  is changed by 46 meV when the polarization of  $YMnO_3$  is reversed. On the basic of the above results, we draw the conclusion that the MnO-terminated heterostructures are endowed with valley-ferroelectricity coupling. The ferroelectricity polarization can be reversed by an electric field, and thus valley polarization can be permanently tuned by switching the ferroelectric polarization of the substrate. The sizable and tunable valley polarization provides a powerful platform for the development of optoelectronic devices based on magnetooptical and magnetoelectric couplings. In addition, the direct band-gap feature of monolayer  $MnPSe_3$  is robust in the MnO-terminated cases, which guarantees the excitation of electrons without loss of momentum. The potential barrier for the ferroelectric polarization reversal is also calculated, which is predicted to be 0.023 eV by comparing

the total energy difference between the ferroelectric state and the transition state (a centrosymmetric MnO termination). Our result is close to the value of 0.012 eV estimated from the experimental coercive electric field for epitaxial  $YMnO_3$  on Pt-sapphire [47].

Unlike monolayer TMDCs, the spontaneous valley polarization of monolayer  $MnPSe_3$  arises from the band renormalization induced by the SOC effect. Mn *d* and Se *p* orbitals play vital roles in the valance band edge characteristics. Hence, the mechanism of valley-ferroelectricity coupling may depend on the controllable orbital hybridization between Se-Mn and the substrate. To gain more insight, the orbital-resolved DOS of MnO-terminated heterostructures is shown in Fig. 6. Mn *d*, Se *p*, I-O *p*, and I-Mn *d* orbitals overlap below the Fermi level. From the DOS analysis of  $MnPSe_3$  components, there are no obvious changes in P and Mn *d* states with the substrate polarization. However, Se *p* states are modulated by polarization, especially for the states below the Fermi level and within the energy range from 1.5 to 2 eV. The variation of  $\Delta_{\text{val}}^V$  is finally reflected in the changes of Se *p* orbitals.

For the MnO-terminated substrate, the first surface MnO layer is selected to extract further information of orbital hybridization. V-Mn is also adopted to show the influence of ferroelectric polarization on the atoms far from the interface. From the DOS analysis of the  $YMnO_3$  substrate, I-O *p* states are significantly modulated in the vicinity of the Fermi level with the reversal of polarization. I-Mn *d*<sub>xy</sub>, *d*<sub>x<sup>2</sup>-y<sup>2</sup></sub> states are slightly influenced. V-Mn *d*<sub>z<sup>2</sup></sub> states in the energy range of 1 to approximately 1.5 eV can also be tailored by polarization, but the states locate above the Fermi level. Thus, the ferroelectric modulation originates from the changes of surface atoms.

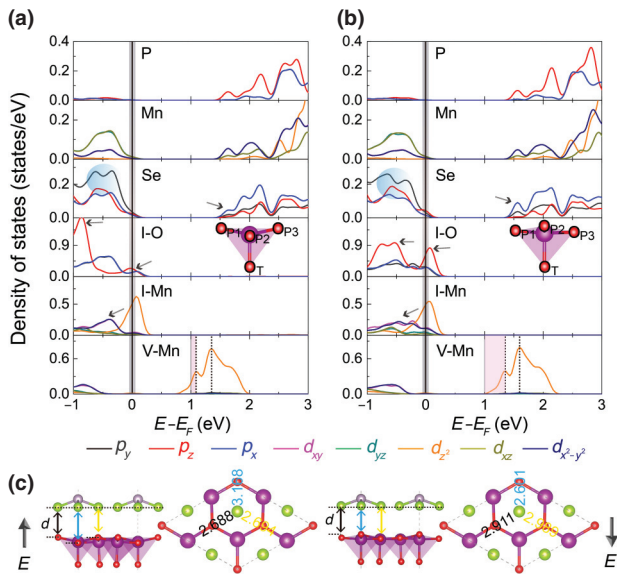


FIG. 6. Orbital-resolved DOS of (a)  $\text{MnO}_{\text{up}}$  and (b)  $\text{MnO}_{\text{dn}}$ . Fermi energy is indicated by the vertical line and set to zero. (c) The variation of O-Se distance and relaxed surface with substrate polarization.  $O_{P1}$ ,  $O_{P2}$ ,  $O_{P3}$ , and  $O_T$  represent the three in-plane and one apical O atoms in  $\text{MnO}_4$  polyhedra, respectively.

The insets are the different relaxations of surface  $\text{MnO}_4$  polyhedra with two polarization directions. One can see that the morphologies of relaxed  $\text{MnO}_4$  polyhedra are associated with the polarization. In Fig. 6(c), the distances between I-O and the bottom Se layer are 2.688, 3.168, and 2.694 Å for  $O_{P1}$ ,  $O_{P2}$ , and  $O_{P3}$  in  $\text{MnO}_{\text{up}}$ , respectively, which are changed by 0.223, 0.567, and 0.295 Å in  $\text{MnO}_{\text{dn}}$ . However, positions of I-Mn atoms are barely altered in these two cases, which is consistent with the DOS results. Hence, the key factor of electrically controlled valley polarization is the variation of O-Se distance with an external electric field, which modulates the orbital hybridization between  $\text{YMnO}_3$  and monolayer  $\text{MnPSe}_3$ .

Finally, in order to verify the mechanism of lattice–ferroelectricity coupling, a vertical strain of  $\pm 5\%$  has been applied to  $\text{MnO}_{\text{up}}$  to see the changes of  $\Delta_{\text{val}}^V$ . In Fig. S2 of the Supplemental Material [46], with the reduction of vertical O-Se distance,  $\Delta_{\text{val}}^V$  are  $-11.3$ ,  $1$ , and  $2.2$  meV in tensile-strained, unstrained, and compressive-strained  $\text{MnO}_{\text{up}}$  models, respectively. The relatively long O-Se distance in the  $+5\%$  system indicates the weak O-Se interfacial hybridization. Hence,  $\Delta_{\text{val}}^V$  of  $-11.3$  meV keeps the same sign and magnitude with the pristine  $\text{MnPSe}_3$  monolayer. When the O-Se distance reaches the equilibrium distance, a small reversed  $\Delta_{\text{val}}^V$  of  $1$  meV appears. The reversed  $\Delta_{\text{val}}^V$  index can be further stabilized to  $2.2$  meV with the O-Se distance continuously decreased. Hence, the concept of electrical control of valley polarization relies on the surface morphology (O-Se distance) modulated by an external electric field.

#### IV. CONCLUSION

In conclusion, the magnetic behavior and electronic states in  $\text{MnPSe}_3/\text{YMnO}_3$  heterostructures are studied based on DFT calculations. The interface structure is closely related to the conductivity of monolayer  $\text{MnPSe}_3$ , which switches the  $p$ - or  $n$ -type doping of  $\text{MnPSe}_3$ . Valley characteristic in valence bands of  $\text{MnPSe}_3$  is destroyed in Y- and O<sub>2</sub>-terminated models due to the strong interfacial hybridization. In particular, the electrically tailored valley polarization is predicted in the  $\text{MnO}$ -terminated heterostructures. The permanent modulation can be achieved by switching the ferroelectric polarization. The determination of electrically controlled valley polarization in monolayer  $\text{MnPSe}_3$  is attributed to the variation of O-Se distance induced by the disordered surface with an external electric field. Additionally, the magnetic behavior of monolayer  $\text{MnPSe}_3$  shows a strong correlation with the ferroelectric polarization and termination of  $\text{YMnO}_3$ . The tunable valley polarization and magnetic behavior in  $\text{MnPSe}_3$ - $\text{YMnO}_3$  heterostructures raise the prospects for electrically controlled valleytronics and boost the development of high-performance memory devices.

#### ACKNOWLEDGMENTS

This work is supported by National Natural Science Foundation of China (Grants No. 51671142 and No. U1632152), Key Project of Natural Science Foundation of Tianjin (Grant No. 16JCZDJC37300).

- [1] D. Xiao, W. Yao, and Q. Niu, Valley-Contrasting Physics in Graphene: Magnetic Moment and Topological Transport, *Phys. Rev. Lett.* **99**, 236809 (2007).
- [2] A. Rycerz, J. Tworzydlo, and C. W. J. Beenakker, Valley filter and valley valve in graphene, *Nat. Phys.* **3**, 172 (2007).
- [3] F. Zhang, J. Jung, G. A. Fiete, Q. Niu, and A. H. MacDonald, Spontaneous Quantum Hall States in Chirally Stacked Few-Layer Graphene Systems, *Phys. Rev. Lett.* **106**, 156801 (2011).
- [4] K. Yang, S. D. Sarma, and A. H. MacDonald, Collective modes and skyrmion excitations in graphene  $SU(4)$  quantum Hall ferromagnets, *Phys. Rev. B* **74**, 075423 (2006).
- [5] R. Akashi, M. Ochi, S. Bordács, R. Suzuki, Y. Tokura, Y. Iwasa, and R. Arita, Two-Dimensional Valley Electrons and Excitons in Noncentrosymmetric  $3R$ -MoS<sub>2</sub>, *Phys. Rev. Applied* **4**, 014002 (2015).
- [6] H. L. Zeng, J. F. Dai, W. Yao, D. Xiao, and X. D. Cui, Valley polarization in MoS<sub>2</sub> monolayers by optical pumping, *Nat. Nanotechnol.* **7**, 490 (2012).
- [7] K. F. Mak, K. L. He, J. Shan, and T. F. Heinz, Control of valley polarization in monolayer MoS<sub>2</sub> by optical helicity, *Nat. Nanotechnol.* **7**, 494 (2012).
- [8] T. Cao, G. Wang, W. Han, H. Ye, C. Zhu, J. Shi, Q. Niu, P. Tan, E. Wang, B. Liu, and J. Feng, alley-selective

- circular dichroism of monolayer molybdenum disulphide, *Nat. Commun.* **3**, 887 (2012).
- [9] A. N. Andriotis and M. Menon, Tunable magnetic properties of transition metal doped MoS<sub>2</sub>, *Phys. Rev. B* **90**, 125304 (2014).
- [10] Y. C. Cheng, Q. Y. Zhang, and U. Schwingenschlögl, Valley polarization in magnetically doped single-layer transition-metal dichalcogenides, *Phys. Rev. B* **89**, 155429 (2014).
- [11] R. Mishra, W. Zhou, S. J. Pennycook, S. T. Pantelides, and J. C. Idrobo, Long-range ferromagnetic ordering in manganese-doped two-dimensional dichalcogenides, *Phys. Rev. B* **88**, 144409 (2013).
- [12] J. Qi, X. Li, Q. Niu, and J. Feng, Giant and tunable valley degeneracy splitting in MoTe<sub>2</sub>, *Phys. Rev. B* **92**, 121403 (2015).
- [13] Q. Zhang, S. A. Yang, W. Mi, Y. Cheng, and U. Schwingenschlögl, Large spin-valley polarization in monolayer MoTe<sub>2</sub> on top of EuO(111), *Adv. Mater.* **28**, 959 (2016).
- [14] N. Singh and U. Schwingenschlögl, A route to permanent valley polarization in monolayer MoS<sub>2</sub>, *Adv. Mater.* **29**, 1600970 (2017).
- [15] T. Maruyama, Y. Shiota, T. Nozaki, K. Ohta, N. Toda, M. Mizuguchi, A. A. Tulapurkar, T. Shinjo, M. Shiraishi, S. Mizukami, Y. Ando, and Y. Suzuki, Large voltage-induced magnetic anisotropy change in a few atomic layers of iron, *Nat. Nanotechnol.* **4**, 158 (2009).
- [16] J. Shen, J. Cong, Y. Chai, D. Shang, S. Shen, K. Zhai, Y. Tian, and Y. Sun, Nonvolatile Memory based on Nonlinear Magnetoelectric Effects, *Phys. Rev. Applied* **6**, 021001 (2016).
- [17] P. Merodio, A. Kalitsov, M. Chshiev, and J. Velev, Electric Field Control of the Resistance of Multiferroic Tunnel Junctions with Magnetoelectric Antiferromagnetic Barriers, *Phys. Rev. Applied* **5**, 064006 (2016).
- [18] Q. Yang, L. Wang, Z. Zhou, S. Zhao, G. Dong, Y. Chen, T. Min, and M. Liu, Ionic liquid gating control of RKKY interaction in FeCoB/Ru/FeCoB and (Pt/Co)<sub>2</sub>Ru/(Co/Pt)<sub>2</sub> multilayers, *Nat. Commun.* **9**, 991 (2018).
- [19] S. Zhao, L. Wang, Z. Zhou, C. Li, G. Dong, L. Zhang, B. Peng, T. Min, Z. Hu, J. Ma, W. Ren, Z. Ye, W. Chen, P. Yu, C. Nan, and M. Liu, Ionic liquid gating control of spin reorientation transition and switching of perpendicular magnetic anisotropy, *Adv. Mater.* **30**, 1801639 (2018).
- [20] N. Sivadas, M. W. Daniels, R. H. Swendsen, S. Okamoto, and D. Xiao, Magnetic ground state of semiconducting transition-metal trichalcogenide monolayers, *Phys. Rev. B* **91**, 235425 (2015).
- [21] X. X. Li, X. J. Wu, and J. L. Yang, Half-metallicity in MnPSe<sub>3</sub> exfoliated nanosheet with carrier doping, *J. Am. Chem. Soc.* **136**, 11065 (2014).
- [22] Q. Pei, X. Wang, J. J. Zou, and W. Mi, Half-metallicity and spin-valley coupling in 5d transition metal substituted monolayer MnPSe<sub>3</sub>, *J. Mater. Chem. C* **6**, 8092 (2018).
- [23] X. Li, T. Cao, Q. Niu, J. Shi, and J. Feng, Coupling the valley degree of freedom to antiferromagnetic order, *Proc. Natl. Acad. Sci. U.S.A.* **110**, 3738 (2013).
- [24] X. Li and J. Yang, First-principles design of spintronics materials, *Natl. Sci. Rev.* **3**, 365 (2016).
- [25] G. Kresse and J. Furthmüller, Efficient iterative schemes for *ab initio* total-energy calculations using a plane-wave basis set, *Phys. Rev. B* **54**, 11169 (1996).
- [26] G. Kresse and D. Joubert, From ultrasoft pseudopotentials to the projector augmented-wave method, *Phys. Rev. B* **59**, 1758 (1999).
- [27] J. P. Perdew, K. Burke, and M. Ernzerhof, Generalized Gradient Approximation made Simple, *Phys. Rev. Lett.* **77**, 3865 (1996).
- [28] S. Grimme, GGA-type density functional constructed with a long-range dispersion correction, *J. Comput. Chem.* **27**, 1787 (2006).
- [29] L. Bengtsson, Dipole correction for surface supercell calculations, *Phys. Rev. B* **59**, 12301 (1999).
- [30] S. L. Dudarev, G. A. Botton, S. Y. Savrasov, C. J. Humphreys, and A. P. Sutton, Electron-energy-loss spectra and the structural stability of nickel oxide: An LSDA+U study, *Phys. Rev. B* **57**, 1505 (1998).
- [31] L. Wang, T. Maxisch, and G. Ceder, Oxidation energies of transition metal oxides within the GGA+U framework, *Phys. Rev. B* **73**, 195107 (2006).
- [32] M. Qian, J. Dong, and D. Y. Xing, Optical properties of the ferroelectromagnet YMnO<sub>3</sub> studied from first principles, *Phys. Rev. B* **63**, 155101 (2001).
- [33] C. J. Fennie and K. M. Rabe, Ferroelectric transition in YMnO<sub>3</sub> from first principles, *Phys. Rev. B* **72**, 100103 (2005).
- [34] B. B. van Aken, T. T. M. Palstra, A. Filippetti, and N. A. Spaldin, The origin of ferroelectricity in magnetoelectric YMnO<sub>3</sub>, *Nat. Mater.* **3**, 164 (2004).
- [35] R. E. Cohen, Origin of ferroelectricity in perovskite oxides, *Nature* **358**, 136 (1992).
- [36] T. Katsufuji, M. Masaki, A. Machida, M. Moritomo, K. Kato, E. Nishibori, M. Takata, M. Sakata, K. Ohoyama, K. Kitazawa, and H. Takagi, Crystal structure and magnetic properties of hexagonal RMnO<sub>3</sub> (*R*=Y, Lu, and Sc) and the effect of doping, *Phys. Rev. B* **66**, 134434 (2002).
- [37] Z. J. Huang, Y. Cao, Y. Y. Sun, Y. Y. Xue, and C. W. Chu, Coupling between the ferroelectric and antiferromagnetic orders in YMnO<sub>3</sub>, *Phys. Rev. B* **56**, 2623 (1997).
- [38] I. V. Solovyev, M. V. Valentyuk, and V. V. Mazurenko, Magnetic structure of hexagonal YMnO<sub>3</sub> and LuMnO<sub>3</sub> from a microscopic point of view, *Phys. Rev. B* **86**, 054407 (2012).
- [39] J. Park, S. Lee, M. Kang, K.-H. Jang, C. Lee, S. V. Streletsov, V. V. Mazurenko, M. V. Valentyuk, J. E. Medvedeva, T. Kamiyama, and J. G. Park, Doping dependence of spin-lattice coupling and two-dimensional ordering in multiferroic hexagonal Y<sub>1-x</sub>Lu<sub>x</sub>MnO<sub>3</sub> (0≤*x*≤1), *Phys. Rev. B* **82**, 054428 (2010).
- [40] K. Kritayakirana, P. Berger, and R. V. Jones, Optical spectra of ferroelectric-antiferromagnetic rare earth manganates, *Opt. Commun.* **1**, 95 (1969).
- [41] V. Grasso and L. Silipigni, Optical absorption and reflectivity study of the layered MnPSe<sub>3</sub> seleniophosphate, *Opt. Soc. Am. B* **16**, 132 (1999).
- [42] A. Wiedenmann, J. Rossat-Mignod, A. Louisy, R. Brec, and J. Rouxel, Neutron diffraction study of the layered

- compounds MnPSe<sub>3</sub> and FePSe<sub>3</sub>, *Solid State Commun.* **40**, 1067 (1981).
- [43] X. Zhang, X. Zhao, D. Wu, Y. Jing, and Z. Zhou, MnPSe<sub>3</sub> monolayer: A promising 2D visible-light photohydrolytic catalyst with high carrier mobility, *Adv. Sci.* **3**, 1600062 (2016).
- [44] Q. Pei, X. Wang, J. Zou, and W. Mi, Tunable electronic structure and magnetic coupling in strained two-dimensional semiconductor MnPSe<sub>3</sub>, *Front. Phys.* **13**, 137105 (2018).
- [45] L. Xu, M. Yang, L. Shen, J. Zhou, T. Zhu, and Y. P. Feng, Large valley splitting in monolayer WS<sub>2</sub> by proximity coupling to an insulating antiferromagnetic substrate, *Phys. Rev. B* **97**, 041405 (2018).
- [46] See Supplemental Material at <http://link.aps.org-supplemental/10.1103/PhysRevApplied.11.014011> for the models of the initial structure and the structure after geometric optimization as well as the band structures of MnO<sub>up</sub> models with different O-Se distances.
- [47] N. Fujimura, H. Sakata, D. Ito, T. Yoshimura, T. Yokota, and T. Ito, Ferromagnetic and ferroelectric behaviors of A-site substituted YMnO<sub>3</sub>-based epitaxial thin films, *J. Appl. Phys.* **93**, 6990 (2003).